

# Tunable Electrical Conductivity of Individual Graphene Oxide Sheets Reduced at “Low” Temperatures

Inhwa Jung,<sup>†</sup> Dmitriy A. Dikin,<sup>\*,‡</sup> Richard D. Piner,<sup>†</sup> and Rodney S. Ruoff<sup>\*,†</sup>

*Department of Mechanical Engineering, University of Texas at Austin, Austin, Texas 78712, and Department of Mechanical Engineering, Northwestern University, Evanston, Illinois 60208*

*Received July 7, 2008; Revised Manuscript Received September 30, 2008*

## ABSTRACT

Step-by-step controllable thermal reduction of individual graphene oxide sheets, incorporated into multiterminal field effect devices, was carried out at low temperatures (125–240 °C) with simultaneous electrical measurements. Symmetric hysteresis-free ambipolar (electron- and hole-type) gate dependences were observed as soon as the first measurable resistance was reached. The conductivity of each of the fabricated devices depended on the level of reduction (was increased more than  $10^6$  times as reduction progressed), strength of the external electrical field, density of the transport current, and temperature.

The study of the electronic properties of graphene and its chemical derivatives promises to open a new era of solid state electronics<sup>1</sup> and of composite materials.<sup>2</sup> A central challenge of rapid graphene implementation is its mass production, and the chemical exfoliation of graphite through oxidation and then dispersion in water, down to single graphene sheets, is one of the potential methods of achieving this goal. Alternative approaches to large-scale production of graphene, such as the thermal exfoliation of graphite oxide<sup>3</sup> and the liquid-phase exfoliation of graphite<sup>4</sup> and expandable graphite<sup>5</sup> powders, are also studied.

While the effect of weak disorder on the electrical conductivity of individual graphene sheets has been intensively studied experimentally<sup>6–9</sup> and theoretically,<sup>10–15</sup> the conductivity of a highly disordered graphene-based material, such as graphene oxide, has only recently attracted attention.<sup>16–25</sup> The main focus of these investigations is to maximize the conductivity of chemically modified graphene sheets by optimizing conditions of chemical and thermal treatments. In this research, we are presenting results of “low”-temperature step-by-step, slow reduction of individual sheets of graphene oxide measured by a 4-probe electrical setup in a combination with a back-gate electrode at a wide variety of source-drain currents, electrical fields, and temperatures. Therefore, the intermediate states of this material are our focus. These results are important for understanding

and controlling the structural and physical properties of graphene oxide and its possible applications.

A sheet of graphene oxide consists of a hexagonal ring-based carbon network having both  $sp^2$ -hybridized carbon atoms and  $sp^3$ -hybridized carbons bearing hydroxyl and epoxide functional groups on either side of the sheet, whereas the sheet edges are mostly decorated by carboxyl and carbonyl groups.<sup>26</sup> Because it is a non-stoichiometric compound, the properties of graphene oxide vary depending on its synthesis, processing, and environmental conditions.

A graphite oxide powder, the starting material prepared for this research, had a carbon-to-oxygen atomic ratio about 2.7, according to our elemental analysis.<sup>27</sup> There are likely also some vacancies (missing carbon atoms), as well as sheet corrugation associated with the local chemical structure.<sup>28</sup> The extensive presence of saturated  $sp^3$  bonds, the high density of electronegative oxygen atoms bonded to carbon, and other “defects” give rise to an energy gap in the electron density of states<sup>25</sup> and makes graphene oxide non-conducting. However, the structural and electronic properties of graphene oxide can be modified by a variety of chemical and thermal processes.<sup>16,18,20–22,24,29</sup> Recently, we have also demonstrated that the optical properties of graphene oxide depend on its level of oxidation.<sup>30,31</sup>

Graphene oxide sheets were prepared as described in ref 32 with only one modification: instead of a short sonication of the graphite oxide–water suspension, we stirred the suspension for a long time (at least one week). As a result, much larger graphene oxide sheets, having lateral sizes up to 100  $\mu\text{m}$ , were found (see Figure 1a,b,c). Single-layer-

\* Corresponding authors. Tel: (847) 467-2024. Fax: (847) 491-3915. E-mail: d-dikin@northwestern.edu. Tel: (512) 471-4691. Fax: (512) 471-7681. E-mail: r.ruoff@mail.utexas.edu.

<sup>†</sup> University of Texas at Austin.

<sup>‡</sup> Northwestern University.

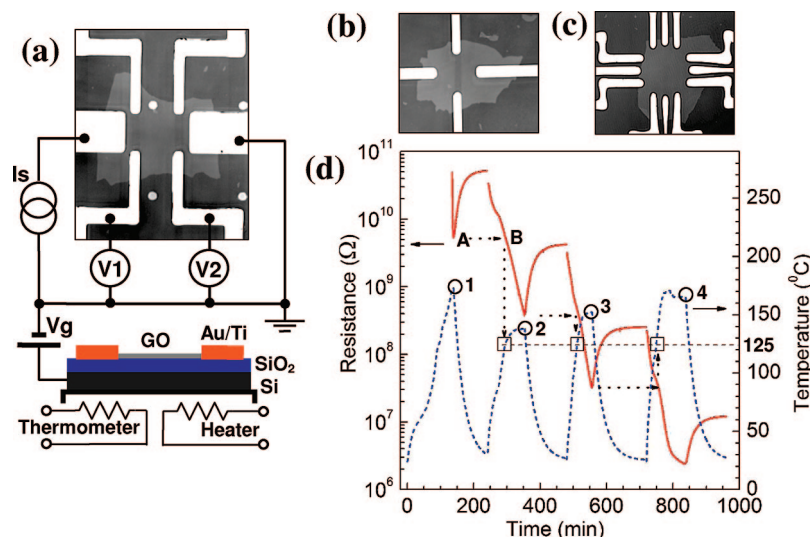


**Figure 1.** Thermal reduction of graphene oxide field effect devices. (a,b,c) Optical images of graphene oxide single sheets with metal leads prepared for conductive measurements. (a) Electrical circuit diagram including Si substrate as a back-gate electrode and mini-hot-plate with incorporated heater and thermometer. (d) Changes in graphene oxide sheet resistance and temperature profile as function of time (sample S12; see Supporting Information for details). The resistance at point A, measured at  $172^{\circ}\text{C}$  (point 1) on the first heating cycle, is equal to that of point B on the second heating cycle, but the temperature at point B is  $125 \pm 5^{\circ}\text{C}$ . A similar behavior (see the three dotted horizontal arrows and the points that they indicate on the heating part of each cycle) was observed for each subsequent cycle during heating, and all three points of sequentially decreasing sample resistance correspond to about the same temperature of  $125^{\circ}\text{C}$ .

thick graphene oxide sheets were easily identified using a confocal microscope, as described in ref 30. Some of the samples were scanned by AFM to ensure that they had a thickness of  $\sim 1$  nm, the thickness of a single layer. A few samples were also characterized by scanning confocal Raman microscopy (see Supporting Information for details).

The differential 4-probe technique and three different layouts of electrodes (separated by 10 to  $50 \mu\text{m}$ ), as shown in Figures 1a,b,c, were fabricated by one-step photolithography with an initial goal of looking for possible anisotropy in individual sheet conductivity. All of the reported electrical measurements were taken in a vacuum chamber ( $\sim 10^{-5}$  Torr) evacuated for at least 1 h prior to the start of the experiment. Eighteen individual graphene oxide devices were measured in total (details in the Supporting Information). The irregular shape of the graphene oxide sheets and the position of the electrodes relative to their edges (van der Pauw configuration) called for data analysis that was performed numerically by using a finite elements method (see Supporting Information for details about device preparation, measurements, and data analysis). Electrical anisotropy in the conductance of the graphene oxide sheets was not observed.

Sample electrical resistance was used as a real-time indicator of graphene oxide chemical/structural modification. By controlling the temperature of the hot plate and the time of heating, we were able to gradually recover the graphene oxide sheet conductivity. Figure 1d shows the temperature profile as a function of time and the corresponding resistance change for one of the samples; a heating rate of  $\sim 1^{\circ}\text{C}/\text{min}$  was used. Four interruptions of heating, with subsequent cool down to room temperature each of the four times, were made at  $172$  (point 1),  $138$  (point 2),  $152$  (point 3), and  $165^{\circ}\text{C}$  (point 4). Data prior to point 1 (Figure 1d) are not shown because no measurable resistance was recorded

until that time. As indicated in Figure 1d, as soon as the “measurable” thermal reduction had begun at about  $160^{\circ}\text{C}$ , reduction continues (resistance decreases) after each repeated cooling and heating as the increased temperature reaches about  $125 \pm 5^{\circ}\text{C}$ . At the fourth heating, the change in the sample resistance exhibited saturation (see red curve approaching minute 800). The sample resistance thus dropped from essentially infinity to about  $2 \text{ M}\Omega$  for this heating protocol.

Current–voltage ( $I$ – $V$ ) curves for this sample measured at room temperature after each step of the heat treatment are nonlinear and slightly asymmetric (Figure 2a). The nonlinearity decreases as the reduction of the graphene oxide progresses. No saturation of the current was ever observed; instead, the sample resistance decreased gradually at increased dc bias. The differential conductance, calculated from the  $I$ – $V$  curves, increases almost linearly with current (Figure 2b); however, this effect depends more on the bias current at a low level of reduction than when the reduction has proceeded further (Figure 2b). Note that the 4-probe configuration excludes the contribution of the metal electrode–sample interface (Schottky barrier) resistances to the sample resistance; thus, the  $I$ – $V$  curves are independent of the contact area or length of the electrodes edges, unlike for a 2-probe configuration.<sup>18,20,22</sup> Charge transport in graphene oxide is thus not contact-limited; instead, it is space-charge-limited, and the injected carriers significantly alter the local electrical field created by the electrode potentials.

On the basis of the sample conductance versus current dependences (as indicated in Figure 2b), the  $I$ – $V$  curves can be fit as  $V(I) = R(I) \cdot I$ , where  $R(I) = (B + A \cdot I)^{-1}$ . Results of such fitting for the second and fourth steps of reduction are shown in Figure 2c,d, with  $B = 5.5 \cdot 10^{-10}$  and  $8.5 \cdot 10^{-8} [\text{S}]$  and  $A = 9.0 \cdot 10^{-3}$  and  $5.7 \cdot 10^{-3} [\text{V}^{-1}]$ , respectively. This

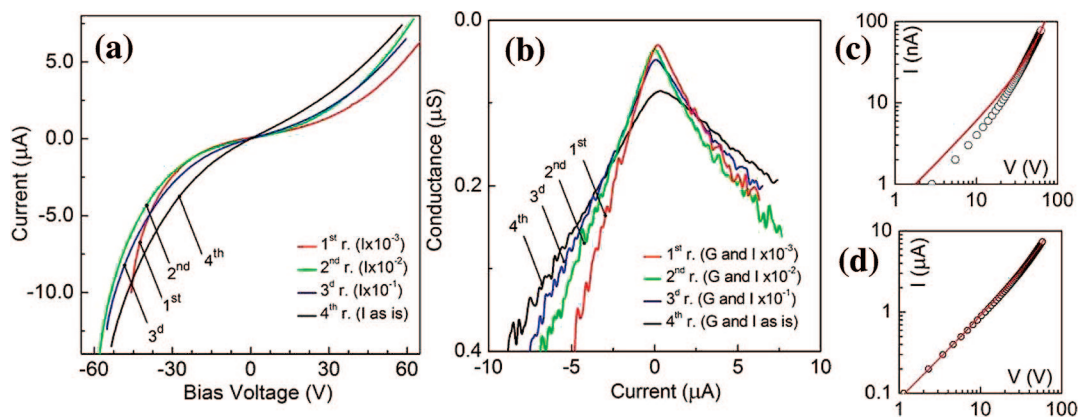


**Figure 2.** Conductivity of a graphene oxide device at different levels of reduction (sample S12). (a) Current–voltage curves recorded at room temperature after each step of consecutive heating shown in Figure 1d. For the unified view of all measured curves, the recorded current  $I$  for first, second, and third steps were multiplied by  $10^3$ ,  $10^2$ , and  $10^1$ , respectively. (b) Differential conductance versus current derived from the set of  $I$ – $V$  curves from panel (a) also with the use of the aforementioned multiplication factors. (c,d) Log–log form of  $I$ – $V$  curves for the second and fourth steps of reduction superimposed with the fitting dependence described in the text.

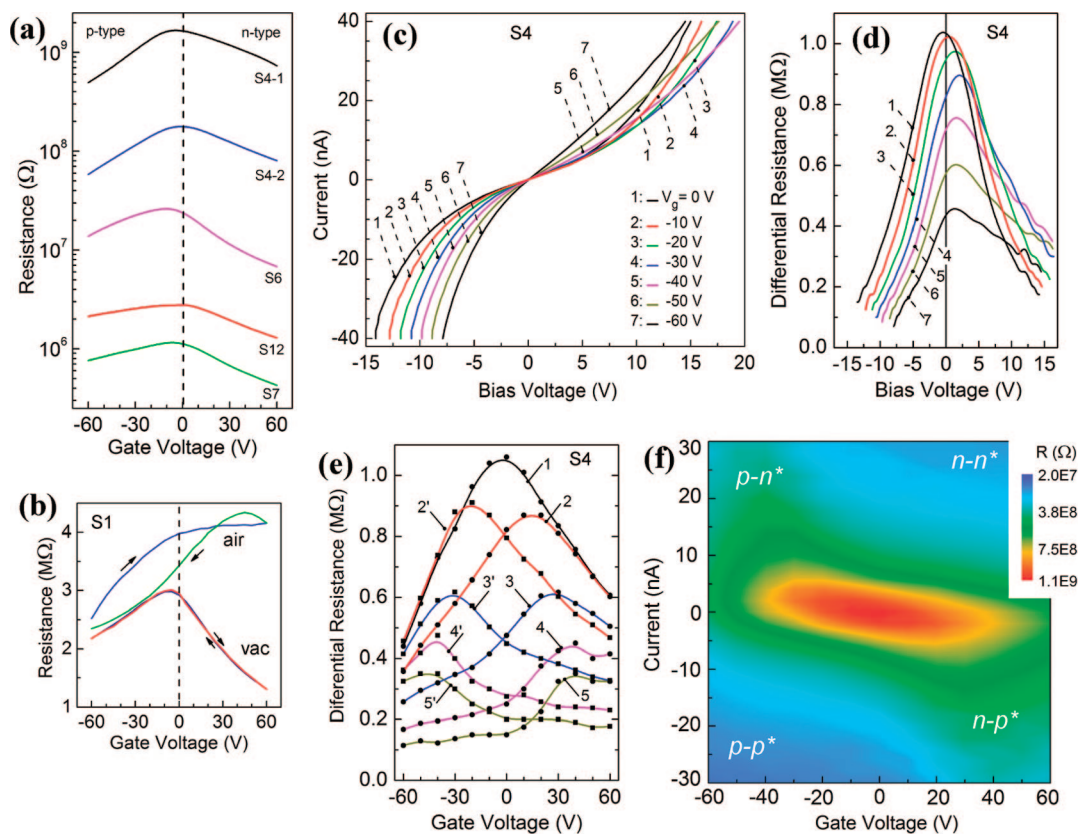


**Figure 3.** Gate and current dependent conductivity of graphene oxide device. (a) Resistance versus gate voltage for 4 different samples, as marked. S4–1 and S4–2 show two reduction states of the same sample. The detailed sample parameters are in Supporting Information. (b) Resistance–gate voltage dependence for S1 in vacuum and after exposure to air. (c)  $I$ – $V$  at different negative gate voltages. (d) Sample resistance derived from  $I$ – $V$  curves in panel (c) and shown at the same gate voltages (curves 1 to 7) as a function of bias voltage. (e) Resistance versus gate voltage recorded at different bias currents:  $I = 0$  (curve 1), +4 and –4 nA (curves 2 and 2'), 10 and –10 nA (curves 3 and 3'), 20 and –20 nA (curves 4 and 4'), 30 and –30 nA (curves 5 and 5'). (f) Color map of the sample resistance as a function of gate voltage and bias current, when p- or n-type of doping is an effect of electric field or (\*) electric charge injection.

approach describes the  $I$ – $V$  data perfectly at the highest level of reduction (Figure 2d), whereas at the early reduction level, some deviation is observed (Figure 2c). Thus, our assumption that graphene oxide conductivity is linearly dependent on the amount of injected charges,  $\sigma \sim I \sim n$ , is correct for the high reduction level.

Surprisingly, once a measurable resistance of the device was achieved, the hysteresis-free back-gate dependent resistance was observed in vacuum (Figure 3a) for all graphene oxide devices, indicating ambipolar and almost symmetric behavior for the electron and hole doping regions, which is similar to graphene.<sup>33</sup> The minimum conductivity points



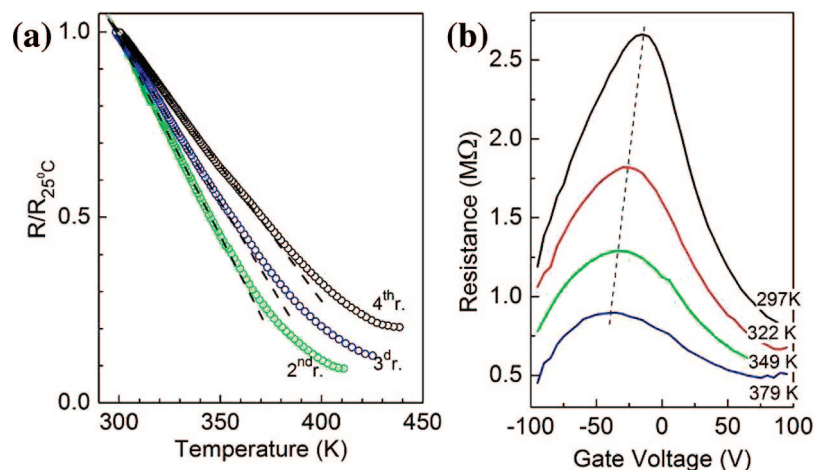


**Figure 4.** Temperature dependences of graphene oxide device. (a) The normalized-to-room temperature sample resistance versus temperature recorded at cooldown as shown in Figure 1d (sample S12). Temperature coefficients of resistance after the second, third, and fourth reductions according to linear fits are  $-11.0 \cdot 10^{-3}$ ,  $-8.9 \cdot 10^{-3}$ , and  $-7.4 \cdot 10^{-3} \text{ K}^{-1}$ , respectively. (b) Resistance as a function of gate voltage measured at 4 different temperatures (sample S12).

(MCP, or the Dirac point) usually had small gate voltage offset (both polarities were observed), despite the fact that the resistivity decays slowly for the entire range of applied fields. This is unlike the behavior of weakly disordered graphene.<sup>6</sup> Any short exposure of graphene oxide devices to the room environment or water vapor led to a rise of hysteretic response to a back-gate potential, since adsorbed molecules, e.g., water, become polarized in the applied electric field (Figure 3b). If the graphene oxide device was placed back in the vacuum chamber ( $10^{-5}$  Torr), the measured hysteresis slowly decreased, but it did not completely vanish until the device was heated to a temperature slightly above  $100^\circ\text{C}$  for approximately 20 min. The remaining chemical groups covalently bound to the carbon skeleton did not reveal any obvious polarization or charging behavior at a relatively slow sweep rate ( $0.1 \text{ V/s}$ ).

Figure 3c,d shows an example of how, initially, almost symmetric n- and p-type conductance was transformed to, e.g., a p-dominated conductance due to a negative gate potential. The same type of transformation was observed via injecting positive or negative charges into a graphene oxide sheet. Subject to these conditions, in both the hole- and electron-accumulation regimes, the  $I$ - $V$  curves become less nonlinear but more asymmetric, as can be seen in Figure 3c. As a result, the MCP moves toward the positive or negative gate potential (see Figure 3e). On the basis of these data, an equivalent change in the carrier charge density per unit-surface due to the “injection doping” of graphene oxide can be estimated. The gate potential, applied across the 300-nm-thick  $\text{SiO}_2$  layer, induces changes in the surface charge density  $n = \epsilon_0 \epsilon V_g / (te) \approx 7.2 \cdot 10^{10} \text{ cm}^{-2}$  per 1 V, where  $\epsilon_0$  and  $\epsilon$  are the permittivity of free space and of the silicon dioxide having thickness  $t$ , and  $e$  is the electron charge. As seen in Figure 3e, 4 nA of injected current leads to a shift of the MCP to +20 or -20 V of the gate voltage, depending on the dc current polarity. Thus, the shift of the MCP can be recalculated as an equivalent change of the charge density in the following way:  $20 \text{ V} \times 7.2 \cdot 10^{10} \text{ cm}^{-2} \text{ V}^{-1} = 1.44 \cdot 10^{12} \text{ cm}^{-2}$ , when a  $\pm 40 \text{ nA}$  bias current corresponds to an MCP

shift of  $\pm 47 \text{ V}$  of the gate voltage and is equivalent to a  $\sim 3.38 \cdot 10^{12} \text{ cm}^{-2}$  change in the carrier density. Following the conventional MOSFET model, when a negative gate potential is applied, a positive dc bias will recover electron loss and restore the n-channel transistor, and a negative dc bias will enhance the p-channel-dominated behavior. The two-dimensional resistance plot (Figure 3f) summarizes the combined effect of n- or p-doping via electrical field and dc bias charge ( $n^*$  or  $p^*$ ) injection. Away from the MCP central area, cooperative p-p\* or n-n\* conductivity enhancement (lower left and upper right corners in Figure 3f) is seen as negative (positive) gate potential and negative (positive) bias, respectively, or as a noncooperative competing contribution of these two factors (upper left and lower right corners in Figure 3f). This behavior looks similar to graphene conductivity controlled by a combination of top and back gates.<sup>34</sup> Thus, both p- and n-carriers are seen in the percolating conductivity of the graphene oxide sheets and their value can be tuned by the gate potential or by charge-injection doping.

The reduced graphene oxide sheet shows a significant increase in resistance upon cooling after each reduction step (Figures 1d and 4a). The likely continued reduction during slow sample cooldown and the narrow temperature interval prohibits more detailed analysis, although one can see that the temperature coefficient of resistance (TCR) is going down as the reduction progresses (see Figure 4a), indicating a decrease in the semiconducting energy gap. The gate-dependent resistance (measured at 1 nA) also exhibits a significant change vs temperature (Figure 4b). Small n-type dominated conductivity at room temperature is transformed upon heating to a much larger electron-doped conductivity with significantly reduced gate dependence. A close similarity with Figure 3d is seen, but in this case, the overall charge transport is controlled by thermal activation instead of carrier injection.

By analogy with a cluster model of amorphous and hydrogenated amorphous carbon,<sup>35</sup> graphene oxide contains both  $\text{sp}^2$  and, predominantly, amorphous  $\text{sp}^3$  sites, and can be described as a quasi two-dimensional amorphous carbon (a-C). A complex set of hydroxyl-hydroxyl and hydroxyl-

epoxide hydrogen-bonding interactions takes place between the functional groups of graphene oxide. The molecular dynamics simulations<sup>36</sup> reveal reactions in which hydrogen atoms are transferred and epoxide groups migrate on the basal plane stabilizing by hydrogen bonding or catalyzing by hydrogen transfer reactions between the mobile epoxide oxygen and neighboring functional groups. Thus, initially the  $sp^2$  clusters in graphene oxide are small and separated by an amorphous and highly disordered  $sp^3$  bonded matrix, which forms a high tunnel barrier between the clusters. During heat treatment, the thermal energy favors the further clustering of the  $sp^2$  phase stimulating connection between ordered rings and moving from amorphous to the two-dimensional nanocrystalline graphene, as was outlined in ref 37. This transformation results in the increase of  $I(D)/I(G)$  ratio and a shift in the position of the  $G$  peak (see Figure 4 in ref 37). The equation for nanocrystalline sizes,<sup>38,39</sup>  $L_a$ , is invalid in this stage of chemically modified graphene (see details in the Supporting Information). However, much more research is required to understand all details of this new material's behavior.

A possible simplified model for the graphene oxide conductance is that of percolation in random continua:<sup>40</sup> the two-dimensional *Swiss-cheese model*. As reduction progresses, a sample-spanning cluster of touching conductive regions is formed, and the sample resistance exhibits a power law decay. That is, the localized states are randomly dispersed throughout the graphene oxide. The model is complicated by the fact that the occupation of the localized states is controlled by the superposition of gate voltage and local electric field created by the amount of injected carriers, and hopping between localized states is thermally assisted. Adequate modeling of such a system will require a host of additional experiments.

Graphene oxide is unique compared to graphene in that its electrical conductivity and optical transparency dramatically depends on the level of oxidation. Such chemically tuned graphene sheets already suggest new vistas<sup>2,18,20,21,41</sup> and hold significant promise for novel sensors, membrane-based NEMS devices, transparent conductors for optoelectronic applications, smart composite materials, and others.

**Acknowledgment.** The authors thank S. Stankovich for making graphite oxide. I.J., D.A.D., and R.S.R. acknowledge funding from the DARPA N/MEMS S&T Fundamentals Program.

**Supporting Information Available:** Fabrication procedure, detailed description of the devices, analysis of their conductivity, and Raman spectroscopy results. This material is available free of charge via the Internet at <http://pubs.acs.org>.

## References

- (1) Geim, A. K.; Novoselov, K. S. *Nat. Mater.* **2007**, *6*, 183.
- (2) Stankovich, S.; Dikin, D. A.; Dommett, G. H. B.; Kohlhaas, K. M.; Zimney, E. J.; Stach, E. A.; Piner, R. D.; Nguyen, S. T.; Ruoff, R. S. *Nature* **2006**, *442*, 282.
- (3) Schniepp, H. C.; Li, J. L.; McAllister, M. J.; Sai, H.; Herrera-Alonso, M.; Adamson, D. H.; Prud'homme, R. K.; Car, R.; Saville, D. A.; Aksay, I. A. *J. Phys. Chem. B* **2006**, *110*, 8535.
- (4) Hernandez, Y.; Nicolosi, V.; Lotya, M.; Blighe, F. M.; Sun, Z.; De, S. T.; M.; Holland, B.; Byrne, M.; Gun'Ko, Y. K.; Boland, J. J.; Niraj,

- P.; Duesberg, G.; Krishnamurthy, S.; Goodhue, R.; Hutchison, J.; Scardaci, V.; Ferrari, A. C.; Coleman, J. N. *Nat. Nanotechnol.* **2008**, *3*, 563.
- (5) Li, X.; Zhang, G.; Bai, X.; Sun, X.; Wang, X.; Wang, E.; Dai, H. *Nat. Nanotechnol.* **2008**, *3*, 538.
- (6) Tan, Y. W.; Zhang, Y.; Bolotin, K.; Zhao, Y.; Adam, S.; Hwang, E. H.; Das Sarma, S.; Stormer, H. L.; Kim, P. *Phys. Rev. Lett.* **2007**, *99*, 246803.
- (7) Cho, S.; Fuhrer, M. S. *Phys. Rev. B* **2008**, *77*, 081402.
- (8) Martin, J.; Akerman, N.; Ulbricht, G.; Lohmann, T.; Smet, J. H.; Von Klitzing, K.; Yacoby, A. *Nat. Phys.* **2008**, *4*, 144.
- (9) Wehling, T. O.; Novoselov, K. S.; Morozov, S. V.; Vdovin, E. E.; Katsnelson, M. I.; Geim, A. K.; Lichtenstein, A. I. *Nano Lett.* **2008**, *8*, 173.
- (10) Pereira, V. M.; Guinea, F.; dos Santos, J.; Peres, N. M. R.; Neto, A. H. C. *Phys. Rev. Lett.* **2006**, *96*, 036801.
- (11) Cheianov, V. V.; Fal'ko, V. I.; Altshuler, B. L.; Aleiner, I. L. *Phys. Rev. Lett.* **2007**, *99*, 176801.
- (12) Fogler, M. M.; Novikov, D. S.; Shklovskii, B. I. *Phys. Rev. B* **2007**, *76*, 233402.
- (13) de Juan, F.; Cortijo, A.; Vozmediano, M. A. H. *Phys. Rev. B* **2007**, *76*, 165409.
- (14) Guinea, F.; Katsnelson, M. I.; Vozmediano, M. A. H. *Phys. Rev. B* **2008**, *77*, 075422.
- (15) Dora, B.; Ziegler, K.; Thalmeier, P. *Phys. Rev. B* **2008**, *77*, 115422.
- (16) Gomez-Navarro, C.; Weitz, R. T.; Bittner, A. M.; Scolari, M.; Mews, A.; Burghard, M.; Kern, K. *Nano Lett.* **2007**, *7*, 3499.
- (17) Wu, X. S.; Li, X. B.; Song, Z. M.; Berger, C.; de Heer, W. A. *Phys. Rev. Lett.* **2007**, *98*, 136801.
- (18) Gilje, S.; Han, S.; Wang, M.; Wang, K. L.; Kaner, R. B. *Nano Lett.* **2007**, *7*, 3394.
- (19) McAllister, M. J.; LiO, J. L.; Adamson, D. H.; Schniepp, H. C.; Abdala, A. A.; Liu, J.; Herrera-Alonso, M.; Milius, D. L.; CarO, R.; Prud'homme, R. K.; Aksay, I. A. *Chem. Mater.* **2007**, *19*, 4396.
- (20) Eda, G.; Fanchini, G.; Chhowalla, M. *Nat. Nanotechnol.* **2008**, *3*, 270.
- (21) Becerril, H. A.; Mao, J.; Liu, Z.; Stoltzenberg, R. M.; Bao, Z.; Chen, Y. *ACS Nano* **2008**, *2*, 463.
- (22) Wu, X. S.; Sprinkle, M.; Li, X. B.; Ming, F.; Berger, C.; de Heer, W. A. *Phys. Rev. Lett.* **2008**, *101*, 026801.
- (23) Li, D.; Muller, M. B.; Gilje, S.; Kaner, R. B.; Wallace, G. G. *Nat. Nanotechnol.* **2008**, *3*, 101.
- (24) Wang, X.; Zhi, L. J.; Mullen, K. *Nano Lett.* **2008**, *8*, 323.
- (25) Boukhalval, D. W.; Katsnelson, M. I. *J. Am. Chem. Soc.* **2008**, *130*, 10697.
- (26) Szabo, T.; Berkesi, O.; Forgo, P.; Josepovits, K.; Sanakis, Y.; Petridis, D.; Dekany, I. *Chem. Mater.* **2006**, *18*, 2740.
- (27) Stankovich, S.; Piner, R. D.; Chen, X. Q.; Wu, N. Q.; Nguyen, S. T.; Ruoff, R. S. *J. Mater. Chem.* **2006**, *16*, 155.
- (28) Cortijo, A.; Vomediano, M. A. H. *Nucl. Phys. B* **2007**, *763*, 293.
- (29) Stankovich, S.; Dikin, D. A.; Piner, R. D.; Kohlhaas, K. A.; Kleinhammes, A.; Jia, Y.; Wu, Y.; Nguyen, S. T.; Ruoff, R. S. *Carbon* **2007**, *45*, 1558.
- (30) Jung, I.; Pelton, M.; Piner, R.; Dikin, D. A.; Stankovich, S.; Watcharotone, S.; Hausner, M.; Ruoff, R. S. *Nano Lett.* **2007**, *7*, 3569.
- (31) Jung, I.; Vaupel, M.; Pelton, M.; Piner, R.; Dikin, D. A.; Stankovich, S.; An, J.; Ruoff, R. S. *J. Phys. Chem. C* **2008**, *112*, 8499.
- (32) Dikin, D. A.; Stankovich, S.; Zimney, E. J.; Piner, R. D.; Dommett, G. H. B.; Evmenenko, G.; Nguyen, S. T.; Ruoff, R. S. *Nature* **2007**, *448*, 457.
- (33) Novoselov, K. S.; Geim, A. K.; Morozov, S. V.; Jiang, D.; Zhang, Y.; Dubonos, S. V.; Grigorieva, I. V.; Firsov, A. A. *Science* **2004**, *306*, 666.
- (34) Williams, J. R.; DiCarlo, L.; Marcus, C. M. *Science* **2007**, *317*, 638.
- (35) Robertson, J.; Oreilly, E. P. *Phys. Rev. B* **1987**, *35*, 2946.
- (36) Paci, J. T.; Belytschko, T.; Schatz, G. C. *J. Phys. Chem. C* **2007**, *111*, 18099.
- (37) Ferrari, A. C.; Robertson, J. *Philos. Trans. R. Soc. Lond., Ser. A: Math. Phys. Eng. Sci.* **2004**, *362*, 2477.
- (38) Tuinstra, F.; Koenig, J. L. *J. Chem. Phys.* **1970**, *53*, 1126.
- (39) Pimenta, M. A.; Dresselhaus, G.; Dresselhaus, M. S.; Cancado, L. G.; Jorio, A.; Saito, R. *Phys. Chem. Chem. Phys.* **2007**, *9*, 1276.
- (40) Balberg, I. *Phil. Mag. B* **1987**, *56*, 991.
- (41) Watcharotone, S.; Dikin, D. A.; Stankovich, S.; Piner, R.; Jung, I.; Dommett, G. H. B.; Evmenenko, G.; Wu, S. E.; Chen, S. F.; Liu, C. P.; Nguyen, S. T.; Ruoff, R. S. *Nano Lett.* **2007**, *7*, 1888.

NL8019938